Early Results from SPARO: Instrument Characterization and Polarimetry of NGC 6334

T. RENBARGER,[1,2] D. T. CHUSS,[1,3] J. L. DOTSON,[4] G. S. GRIFFIN,[5] J. L. HANNA,[1,6] R. F. LOEWENSTEIN,[7] P. S. MALHOTRA,[1,8]
J. L. MARSHALL,[1,9] G. NOVAK,[1] AND R. J. PERNIC[7]

ABSTRACT. The Submillimeter Polarimeter for Antarctic Remote Observations (SPARO) employs two nine-element arrays of ^{3}He-cooled bolometers to measure linear polarization at $\lambda = 450$ μm. It is operated at the focal plane of the Viper telescope, located at the Amundsen-Scott South Pole Station. SPARO obtains better sensitivity to degree-scale polarized submillimeter emission than can be currently achieved with any other experiment. We describe the design of SPARO's optics, detectors, and electronics. We also review the design of the SPARO cryostat, which has already been discussed in a previous paper. We discuss the performance of SPARO and Viper during observations at the South Pole in 2000, and we present polarimetric observations of NGC 6334 made with SPARO. Finally, we compare these observations with submillimeter polarimetric observations of the same source made at the Caltech Submillimeter Observatory and the James Clerk Maxwell Telescope, and we discuss the implications of these three data sets for the magnetic field in NGC 6334.

1. INTRODUCTION

Interstellar dust grains are rapidly spinning, are usually cold, and are often aligned with respect to the ambient interstellar magnetic field (Lazarian 2000). When aligned, they emit linearly polarized thermal radiation in the submillimeter band, thereby providing a method for measuring the direction of the interstellar magnetic field as projected onto the plane of the sky. Submillimeter polarimetry of molecular clouds can thus provide tests for theories of star formation.

In regions of active star formation, the field geometry will be affected by the formation process. A strategy relying solely on observations of active sites to inform models of star formation will therefore be incomplete. One way to fill in the gaps is to map fields in regions that are gravitationally bound but lack a central protostar (Ward-Thompson et al. 2000). A second strategy is to map magnetic fields on large scales. The large-scale field will be relatively unchanged by star formation and

will provide a baseline field direction for comparison with the field geometry in the active sites.

Two submillimeter observatories on Mauna Kea, the Caltech Submillimeter Observatory (CSO, 10 m primary) and the James Clerk Maxwell Telescope (JCMT, 15 m primary), are used for polarimetric observations with angular resolution in the range of 15″–20″. The Submillimeter Polarimeter for Antarctic Remote Observations (SPARO) is used with the Viper telescope (2 m primary), located at the Amundsen-Scott South Pole Station. SPARO makes use of only the inner 0.7 m of Viper's primary and obtains an angular resolution of about 4′. Its primary goals are to map large-scale magnetic fields in star-forming molecular clouds and to map the large-scale magnetic field at the Galactic center. Due to the advantages of the South Pole as a submillimeter site (Lane 1998) and to the fact that Viper is optimized for large-scale mapping, SPARO provides the best sensitivity to degree-scale emission of any submillimeter polarimeter currently in operation. Thus, SPARO observations are complementary to submillimeter polarimetric observations made using the large telescopes on Mauna Kea.

SPARO incorporates two ^{3}He-cooled detector arrays, each of which includes 9 pixels arranged in a 3 × 3 pattern. We use two arrays so we can simultaneously observe two orthogonal components of linear polarization. A number of design elements from the submillimeter polarimeters Stokes (Platt et al. 1991) and Hertz (Schleuning et al. 1997; Dowell et al. 1998) were incorporated into the SPARO design. The best observing conditions at the South Pole occur during the winter, when the station is being run by a small isolated crew, no flights in or out of the station are possible, and the ambient temperature often drops below −100 F. In order to maximize our chances of success under these conditions, the SPARO cryostat was

---

[1] Department of Physics and Astronomy, Northwestern University, 2145 Sheridan Road, Evanston, IL 60208; renbarge@physics.umn.edu.

[2] Department of Physics and Astronomy, University of Minnesota, Minneapolis, MN 55455.

[3] NASA Goddard Space Flight Center, Greenbelt, MD 20771.

[4] NASA Ames Research Center, MS 245−6, Moffett Field, CA 94035.

[5] Department of Physics, Carnegie Mellon University, 5000 Forbes Avenue, Pittsburgh, PA 15213.

[6] NASA Langley Research Center, Hampton, VA 23681.

[7] Yerkes Observatory, University of Chicago, 373 West Geneva Street, Williams Bay, WI 53191.

[8] School of Medicine, Case Western Reserve University, Cleveland, OH 44106-7215.

[9] Department of Astronomy, Ohio State University, 140 West 18th Avenue, Columbus, OH 43210.
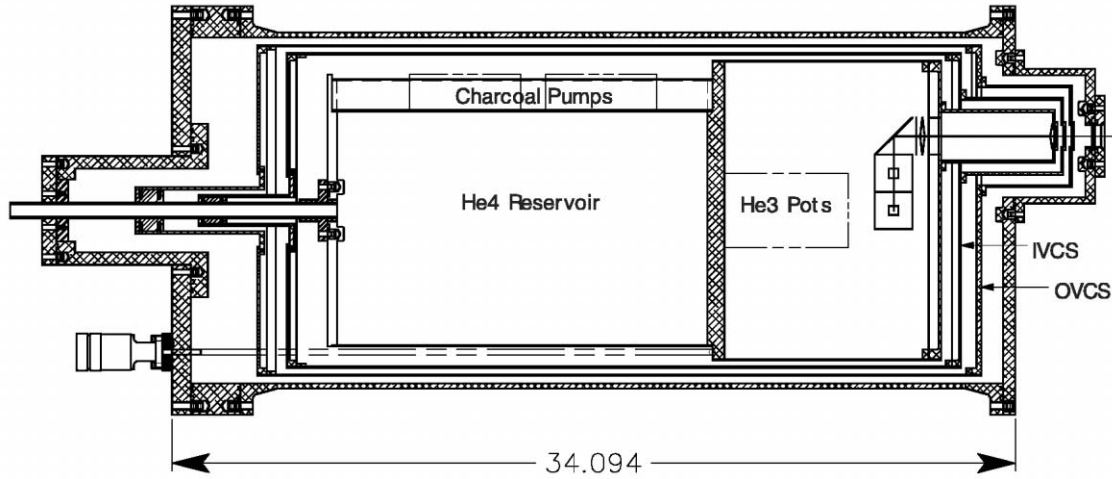
Fig. 1.—Scale drawing of SPARO cryostat. SPARO has a cylindrical shape shown here in cross section. The inner and outer vapor-cooled radiation shields (IVCS and OVCS) surround the liquid ^{4}He reservoir and are thermally connected to the ^{4}He fill tube. During observations, the instrument is rotated clockwise from the orientation shown here, by 30°–90°, depending on the source elevation. There are two ^{3}He pots: a guard stage at 0.4 K and an inner stage at 0.3 K that cools the detectors. These are pumped by two charcoal adsorption pumps. A thin capillary leads from the ^{4}He reservoir to a continuously filled pumped pot, which is maintained at 1.5 K. The capillary and pumped pot are not shown. They are located near the ^{3}He pots. Radiation enters SPARO through a snout (*upper right*), along an optic axis that is offset from the cryostat's center line. A sketch of the optics and detectors can be seen just inside the snout (see also Fig. 2). The linear dimension is given in inches.

designed with an eye toward simplifying the regular cryostat servicing operations and/or reducing their frequency. The cryostat design has been described by Dotson et al. (1998).

SPARO's first overwinter observations were made during the 2000 austral winter. The main target was the Galactic center, which we observed for about 5 weeks. The Galactic center results have been reported by Novak et al. (2003). We also spent a shorter time during the 2000 austral winter observing the star-forming molecular cloud NGC 6334. In this paper, we report on the design and performance of the SPARO instrument and on the NGC 6334 observations. At the time of this writing, SPARO's second South Pole overwinter (2003 austral winter) is under way.

In § 2 we review the design of the cryostat and describe its performance during South Pole observations. The design and specifications of the optics, detectors, and electronics are covered in § 3. In § 4 we discuss the results of laboratory tests of SPARO. We cover the performance of the integrated SPARO/Viper system in § 5. Finally, in § 6 we present our NGC 6334 observations and compare them with submillimeter polarimetric observations of this source made from the CSO and JCMT.

2. CRYOSTAT

Figure 1 illustrates the SPARO cryostat and optics. SPARO's 4 K stage is surrounded by two radiation shields that are thermally connected to the ^{4}He fill tube and thus are cooled by helium vapor. They are referred to as the inner and outer vapor-cooled shields (IVCS and OVCS). SPARO has a ^{4}He hold time of 3.5 days when operated in a 300 K environment, and 5–6

days when operated on the Viper telescope in winter at ambient temperatures near 200 K. The IVCS and OVCS have respective temperatures of 80 K and 170 K when SPARO is in a 300 K environment.

The SPARO ^{3}He refrigerator is a self-contained, dual-stage system. The ^{3}He hold time of 3.5 days is limited by the outer stage, which contains 22 liters STP of gas. A pumped ^{4}He pot inside SPARO provides a 1.5 K stage, thus allowing for recondensation of ^{3}He without pumping on the main ^{4}He reservoir. The pumped pot is pumped continuously via a pumping line that runs through the telescope's cable wrap to a mechanical pump. It is also supplied continuously via a capillary connecting it to SPARO's main ^{4}He reservoir. The only outdoor operation that is needed during the recondensing cycle is manipulation of a mechanical heat switch that is used to sink the charcoal adsorption pumps to 4 K.

Based on the displacement rate of the mechanical pump and the pressure in the pumping line, one can determine the molar flow rate through the capillary. From this, one can calculate the cooling power of the pumped pot (deLong et al. 1971). In practice we observe that the pressure in the pumping line is variable, which implies variable molar flow rate, and thus variable cooling power. This variability is not understood but may be related to partial plugging of the capillary by frozen air. Because of the variable cooling power, the time required for recondensation of ^{3}He also varies, ranging from 0.5 to 1.5 days.

The molar flow rate through the capillary varies between 4×10^{-5} mol s^{-1} and 5×10^{-4} mol s^{-1}. The latter value is close to the design specification. We made a direct measurement of the cooling power using the procedure described by Dotson

et al. (1998), at a time when the molar flow rate was near the low end of its range. This measured cooling power agrees well with that calculated from the molar flow rate. Finally, we note that the fact that the molar flow rate is variable provides a good explanation for the unexpectedly low cooling power found by Dotson et al. (1998) during initial testing of the pumped pot.

In order to minimize the heat load on the pumped pot during ^{3}He recondensation, we attempted to heat sink the ^{3}He gas to 4 K at a point between the charcoal pumps and the pumped pot. Based on measured condensing times and calculated cooling power values, it is possible to estimate the temperature of the ^{3}He gas as it comes into contact with the pumped pot. Using the ideal gas law and the known latent heat, we calculate that this temperature is 14–20 K. Thus, the heat sinking to 4 K is not fully effective. Better heat sinking might result in a reduction in the duration of the recondensing phase.

Due to the low ambient temperature, we chose to use indium seals and copper gaskets instead of elastomer O-rings to seal the cryostat's vacuum space (Dotson et al. 1998). There is one exception: the seal to the quartz pressure window is accomplished using a heated silicone O-ring.

3. OPTICS, DETECTORS, AND ELECTRONICS

The SPARO optics, detectors, and electronics are patterned after those of two previous array polarimeters developed at the University of Chicago for far-infrared and submillimeter wavelengths: Stokes (Platt et al. 1991) and Hertz (Schleuning et al. 1997; Dowell et al. 1998). Like Stokes and Hertz, SPARO employs re-imaging optics (Hildebrand 1985). Typically, two lenses accomplish the re-imaging: a field lens at the telescope's focal plane re-images the primary to a pupil lens, which re-images the focal plane onto the detectors. A rotating, birefringent half-wave plate serves to modulate the polarization. This half-wave plate is placed near the pupil lens, as are some of the spectral filters. By keeping these elements near an image of the primary mirror, systematic errors in polarimetry are reduced (Platt et al. 1991; Gonatas et al. 1989). A free-standing wire grid located between the pupil lens and the detectors serves to split the radiation into two orthogonal polarization components. Each component is then detected by a separate detector array.

The detector arrays used in SPARO are similar to those used in Stokes and Hertz. For all three instruments, the detectors are semiconducting bolometers, with each bolometer mounted by hand into its own reflective cylindrical cavity. Each detector has a corresponding ideal light concentrator of compound parabolic design (Winston 1970) mounted to the cavity opening. The detector arrays are cooled to ∼0.3 K, and all remaining optical elements are cooled to 4 K, except for blocking filters mounted to radiation shields.

Table 1 lists characteristics for SPARO's filters, lenses, half-wave plate, light concentrators, and detectors. The optics were upgraded between the 2000 and 2003 overwinter seasons (see

§ 4). Figure 2 shows two detailed views of SPARO's cold (0.3–4 K) optics. Before reaching the cold optics, incident radiation passes through a diamond-dust-coated quartz pressure window and one or more low-pass blocking filters that are mounted to the vapor-cooled shields (the configuration of blocking filters was changed for 2003 as listed in Table 1). These elements are not shown in Figure 2. Another low-pass filter (BLF in Fig. 2) is placed directly in front of the field lens (FL). SPARO's lenses (FL, PL) and half-wave plate (HWP) are constructed of crystal quartz. The wire grids (G1, G2) are made of gold-plated tungsten wires and were purchased from QMC Instruments, Ltd., Cardiff, UK.

The second grid (G2) is used instead of a mirror in order to provide additional purification of the transmitted polarization component. It can be tilted in order to ensure that each pixel in the T array will observe the same sky position as the corresponding pixel in the R array (see Fig. 2). This small adjustment is needed to correct any error in the alignment of the detector arrays and can be carried out while the instrument is cold via a system of shafts and gears leading from the grid to a mechanical vacuum feed-through. We decided that vertical alignment of the arrays could be achieved with careful construction, leaving horizontal alignment as the sole adjustment. During operation at the South Pole in 2000, the horizontal alignment error was measured to be 0.04 of the pixel separation, and vertical alignment error was 0.09 of the pixel separation.

SPARO's detectors are NTD Ge bolometers that have dimensions of $0.25 \times 0.25 \times 0.30$ mm, with 25 μm diameter NbTi leads. Each of SPARO's two detector arrays has nine bolometers arranged in a 3×3 square pattern, and operates at 285 mK. We have carried out laboratory measurements of bolometer responsivity in Volts/Watt (V/W), as determined by the I-V characteristics of the bolometers (Mather 1984; Dowell et al. 1998). We did this measurement with the bolometers exposed to a cold load provided by a 4 K internal blank-off wheel, and also for a warm load provided by opening the blank-off wheel to admit 300 K radiation from the laboratory. The detector responsivity during actual observations (load temperature ∼200 K) must lie between these two measured values. Table 1 gives the measured responsivities for these two conditions as well as a simple interpolation providing an estimate of the responsivity during observations. Note that the lower warm load responsivity for 2003 is expected, as the improved optical efficiency (see § 4) leads to greater loading of the bolometers.

Tensioned manganin wires 51 μm in diameter carry the signals from each detector array to the 4 K work surface. For each detector array, one set of wires bridges the temperature gap between the bolometers and the guard ^{3}He stage, while a second set of tensioned wires leads from the guard stage to a printed circuit (PC) board mounted to the 4 K surface. Leaf springs attached to the ends of each set of wires provide the tension, which serves to reduce low-frequency, vibration-induced capacitive pickup.

Each of the two PC boards on the 4 K work surface carries

TABLE 1
Characteristics of SPARO

Characteristic	2000 Austral Winter	2003 Austral Winter
Detector responsivity (V/W):		
Cold load	5.0×10^8	No change
300 K load	3.8×10^8	2.1×10^8
200 K load (estimated)	4.1×10^8	2.9×10^8
Detector NEP (electrical; W Hz$^{-0.5}$)	1.2×10^{-16}	No change
Detector time constant (optical; ms)	20	No change
Pixel spacing (mm)	3.2	No change
f/# of Winston cones	f/3.5	No change
Center of passband (λ_0; μm)	450	No change
$\Delta\lambda/\lambda_0$	0.1	No change
Field lens specifications:		
Shape	Plano-convex	No change
Focal length (mm)	119	No change
Diameter (mm)	25 (~19 clear)	No change
Pupil lens specifications:		
Shape	Bi-convex	No change
Focal length (mm)	67	No change
Diameter (mm)	45 (~42 clear)	No change
Lens spacing (mm):		
Field lens to pupil lens	~133	No change
Pupil lens to detectors	~133	No change
Half-wave plate thickness (mm)	4.6	No change
Blocking filters:		
At OVCS[a] (170 K)	Black polyethylene	...
At IVCS[a] (80 K)	IR Labs[b] C170 (170 μm cut-on)	QMCI[c] chemical filter (180 μm cut-on)
At 4 K shield	QMCI chemical filter (180 μm cut-on)	QMCI interference filter (300 μm cut-on)
Optical efficiency	<2.6%	8.2%
Polarization efficiency	>85%	No change

[a] See Fig. 1.
[b] Infrared Laboratories, Tucson, AZ.
[c] QMC Instruments, Cardiff, Wales.

its signals to a corresponding junction field effect transistor (JFET) box. The two JFET boxes are also mounted directly to the 4 K surface. Each box contains nine source followers that serve as unity gain impedance transformers (see Dowell et al. 1998 for circuit diagram), with the JFETs mounted onto a single PC board that is kinematically suspended for thermal isolation and heated to 135 K. The suspension uses spring loading via thin-walled G-10 tubing and small-diameter Kevlar thread. The design is similar to that described by Ruhl (1993). To bridge the temperature gaps at the two ends (input and output) of the PC board, we again use tensioned wires and leaf springs. The JFETs are dual-package, type InterFET 2N6451, and are heated by their own power dissipation. The drain voltage and current are 5 V and 0.6 mA, for a total heat input of about 27 mW for each nine-channel JFET box.

Low-noise preamplifiers are mounted to the exterior of the cryostat. A 16 bit data system, mounted in a heated box on the telescope frame, converts the analog signal to digital. Fiber optics carry the signal from the analog-to-digital conversion system to the Macintosh Quadra data computer, located in the telescope control room. The data acquisition scheme involves making short photometric observations at each of six half-wave plate angles. Each such photometric observation is obtained by combining fast (~3 Hz) chopping of Viper's chopping flat mirror (see § 5) with slow (~0.1 Hz) nodding of the telescope. This procedure is described in detail by Hildebrand et al. (2000).

4. LABORATORY TESTS

Figure 3 shows a top view of the optical test bench that we used for a series of optical tests of SPARO conducted at Northwestern University in 1998. A commercial blackbody source emits radiation that passes through a rotary chopping wheel, and an off-axis paraboloidal mirror collimates the chopped radiation. A flat mirror bends the optical path into a second off-axis paraboloidal mirror that focuses the light upward through the aperture of an instrument rotator and into SPARO. The instrument rotator sits horizontally, with its axis of rotation oriented vertically. During testing, SPARO is bolted to the rotator so that its optical snout (see Fig. 1) protrudes through the aperture of the rotator, and its field of view extends downward toward the focusing mirror. The inclusion of an instrument rotator allowed us to make precise measurements of the in-
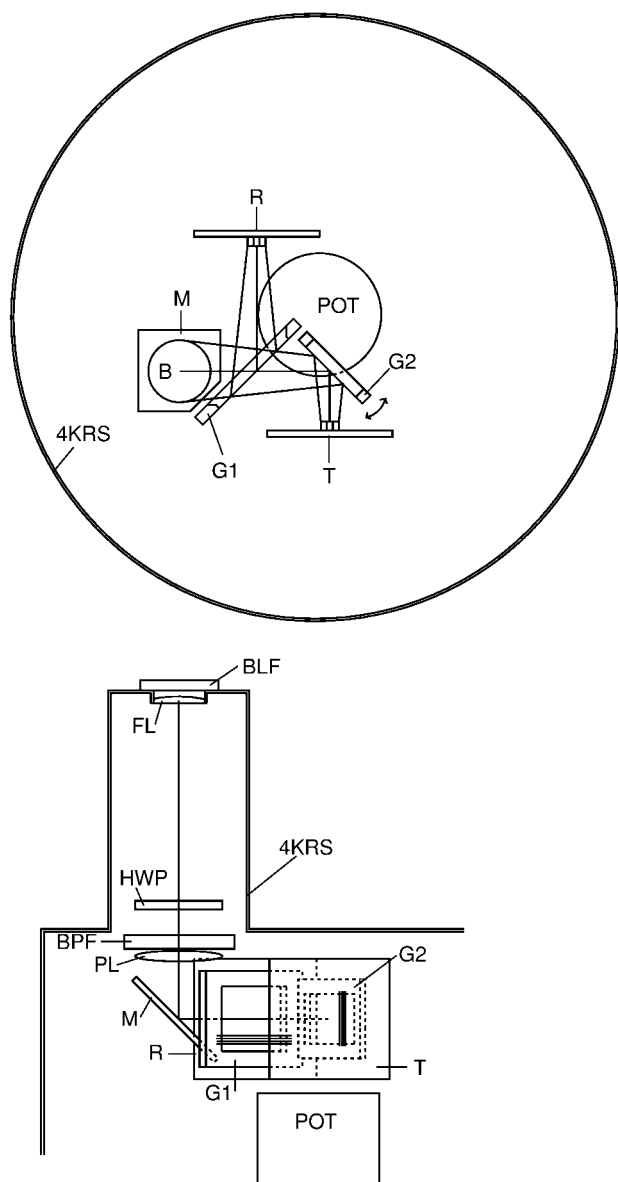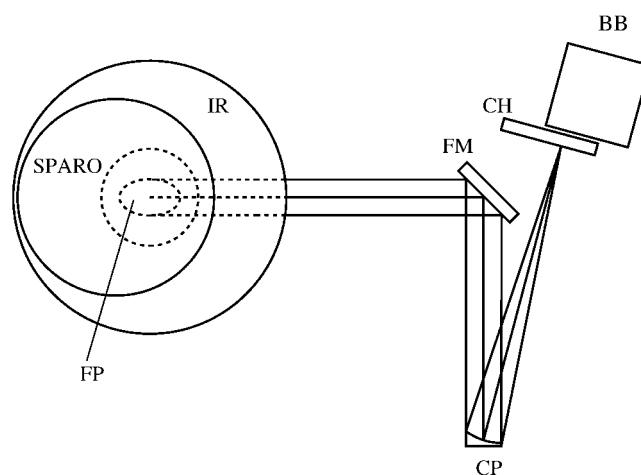
FIG. 3.—Diagram of optical test bench (top view). Radiation emitted horizontally by a blackbody source (BB) is modulated by a chopping wheel (CH). The collimating paraboloidal mirror (CP) directs collimated radiation toward a flat mirror (FM). FM deflects the (still horizontal) collimated beam toward the focusing paraboloidal mirror (FP), located underneath an instrument rotator (IR). FP deflects the optic axis by 90° so that the focused beam of radiation is directed upward (toward the reader) through an aperture (*dashed circle*) in IR and into SPARO. Radiation enters SPARO through its off-center snout (see Fig. 1). The snout (not shown) fits just inside the aperture in IR. The rotation axis of IR is vertical and passes through the center of FP.

FIG. 2.—Diagram of the SPARO cold (4 K) optics. The upper illustration shows the view from the perspective of photons entering SPARO's snout (see Fig. 1). The large circle (4KRS) is the 4 K radiation shield that surrounds the optics and is concentric with the cylindrical outer case of SPARO. The axis of SPARO's snout is at the center of the circle marked B. The lower illustration is a side view, with the snout pointed upward. (However, during operation the snout points downward or sideways.) Radiation enters the cold optics through the blocking filter (BLF) and then passes through the field lens (FL), the rotating half-wave plate (HWP), the bandpass filter (BPF), and the pupil lens (PL). Next, the beam is reflected by the mirror (M) toward the grids. The circle at B shows the beam size at M. A polarizing grid (G1) splits the beam of radiation into two orthogonal polarization components. The reflected component is detected by the R array (R). The component transmitted by G1 is reflected by a second grid (G2) and then detected by the T array (T). For both G1 and G2, the lower illustration shows a few of the grid wires. The degree of freedom for adjustment of G2 is indicated in the upper illustration. The detector arrays are mounted to the innermost of the two ³He pots (POT). The outer ³He pot is not shown.

strumental polarization. The test bench was also used to adjust the tilt of the second grid (G2 in Fig. 2), and to measure other optical parameters such as polarization efficiency and beam size.

For both the 2000 and 2003 optical configurations (see Table 1), the optical efficiency of SPARO was estimated from measurements of the bolometer I-V curves under different radiative loading conditions. Specifically, we measured the I-V curves with the bolometers exposed to a 4 K radiation load (internal blank-off wheel in closed position) and again with the bolometers exposed to a 300 K radiation load (blank-off wheel open; 300 K absorber in front of pressure window). If we assume for the moment that all optical elements in SPARO are either at 4 K or 300 K, then the optical efficiency can be easily derived as follows:

First, the 4 K and 300 K I-V curves for each bolometer are analyzed together to determine the power that is incident upon the bolometer when it is under the 300 K load (e.g., see Dowell et al. 1998). Next, this power level is divided by the power that would be expected from a 300 K blackbody filling the field of view of the bolometer (but divided by 2 to account for the polarization splitting). This yields the optical efficiency of the 4 K optics. This value is then corrected by the separately measured transmission of the 300 K optics to determine the total optical efficiency.

All of our computations of optical efficiency are carried out under this two-temperature idealization. Specifically, the filter (if any) at the OVCS is taken to be at 300 K instead of

170 K, and the filter at the IVCS is taken to be at 4 K instead of 80 K. If these intermediate-temperature filters have high transmission, then our two-temperature idealization does not introduce much error. For the 2003 optical configuration, the one filter used at intermediate temperature has a high transmission (80% at 80 K), and the computed optical efficiency is accurate. However, the filter we used at the IVCS in 2000 has an unknown and possibly low transmission at 80 K, as it was designed for use at 4 K. (It was due to an oversight that we used this filter at the IVCS.) For this reason the computed optical efficiency for the 2000 configuration represents only an upper limit (see Table 1). The large improvement in optical efficiency between 2000 and 2003 is due to the use of better low-pass filters (see Table 1) and the application of better antireflection coatings to the quartz optics.

5. OVERALL PERFORMANCE

In this section, we assess the overall performance of the integrated SPARO/Viper system, based on observations made during the 2000 austral winter. The Viper telescope, located at the Amundsen-Scott base at the South Pole, is an off-axis telescope with a 2 m diameter primary mirror. It has been used mainly for cosmic microwave background anisotropy measurements (Peterson et al. 2000). The relatively small diameter of the Viper primary limits our angular resolution to several arcminutes, but the large throw of Viper's flat chopping mirror (corresponding to several degrees in azimuth on the sky) facilitates the detection of spatially extended flux. When SPARO is installed on Viper, we use a substitute "condensing mirror," which results in 0.7 m primary mirror illumination for SPARO's f/3.5 optics.

Based on the design, we expect a beam size of about $4\rlap{.}'0$ FWHM. This estimate is derived by quadrature addition of $3\rlap{.}'0$, corresponding to the 3.05 mm entrance aperture of the Winston concentrator, and $2\rlap{.}'7$, corresponding to the FWHM of the Airy disk. We were not able to measure SPARO's beam size accurately, because of a lack of available point sources, but we were able to set an upper limit of $6'$ on the beam FWHM by observing NGC 6334 I/I(N) and RCW 57. We measured a pixel separation of $3\rlap{.}'5$.

We next describe how we are able to use SPARO observations of NGC 6334 I/I(N) to constrain the optical efficiency of the Viper telescope. First, we estimate the flux received at Viper by integrating the 400 μm map of NGC 6334 I/I(N) made by Gezari (1982) over the area of SPARO's beam, here assumed to be $4'$ FWHM. The 400 μm flux is corrected to 450 μm using the Rayleigh-Jeans approximation and assuming a grain emissivity proportional to the inverse square of the wavelength (Hildebrand 1983). We find that for NGC 6334 I/I(N), the ratio of the average flux measured in SPARO's corner pixels to the flux measured in the central pixel is 30%. The corner pixels have separations from the central pixel comparable to the chop-

per throw used by Gezari (1982). Thus, Gezari's measurements can be expected to underestimate the SPARO flux by a factor of about 1.3. We correct accordingly. The correction for atmospheric absorption is done using the zenith opacity measurements obtained by the NRAO-CMU 350 μm opacity monitor. For this purpose, we assume that the opacity in SPARO's 450 μm passband is the same as that in the 350 μm passband of the opacity monitor.

To obtain the optical efficiency of Viper, we compare the value for the flux incident on Viper, obtained as described above, with the flux measured by SPARO. In calculating the latter, we take into account the AC correction to SPARO's responsivity ($\eta \sim 0.9$), which arises as a combination of the chop frequency (3.1 Hz) and the finite time constant of the bolometers (Mather 1984). We also correct for the chopper duty cycle ($\eta \sim 0.85$). Assuming a SPARO optical efficiency of 2.6% (see Table 1), the result of this calculation is a telescope efficiency of 50% $\pm$ 15%. However, 2.6% is actually an upper limit, so we conclude that we have placed a lower limit of 35% on the optical efficiency of the Viper telescope. The theoretically expected telescope optical efficiency at 450 μm is 80%. This is based on an estimate of Ruze (1953) scattering losses due to the combined surface errors of all four of Viper's mirrors (15 μm rms).

We estimate a noise-equivalent flux density (NEFD) of about 1000 Jy for SPARO, based on polarimetric observations of the Galactic center. This estimate is referenced to a 450 μm zenith opacity of unity and an elevation of $45°$, or a product of zenith opacity and air mass (cosecant of elevation) of $\sqrt{2}$. We have compared this performance to that obtained by the Hertz instrument at the Caltech Submillimeter Observatory (CSO). The Hertz NEFD of 4 Jy (Dowell et al. 1998) is referenced to a product of 350 μm zenith opacity and air mass equal to 1.5. The CSO has a 10 m primary that Hertz completely illuminates, while SPARO illuminates only 0.7 m of the Viper primary. Because NEFD scales inversely with the area of the primary, the 4 Jy NEFD for the Hertz/CSO combination would correspond to 900 Jy if referenced to a 0.7 m diameter primary. Thus, the performance of SPARO is roughly comparable to Hertz, as expected given the similarities in design and specifications of the two instruments. We expect that our ongoing 2003 austral winter observations with SPARO will yield a lower NEFD as a result of the better optical transmission in 2003 (see Table 1).

Viper is an off-axis telescope, so it is expected to cause some spurious polarization. This effect should be about 0.3% in magnitude (Renbarger et al. 1998). During the 2000 winter, we determined the combined SPARO/Viper instrumental polarization in two ways. The first was based on SPARO polarimetry of the intensity peak of Sagittarius B2. We averaged higher angular resolution observations of Sgr B2 made at 350 μm (Dowell et al. 1998) over the area of SPARO's beam, assumed to be $4'$ in diameter. This procedure yields a polarization mag-
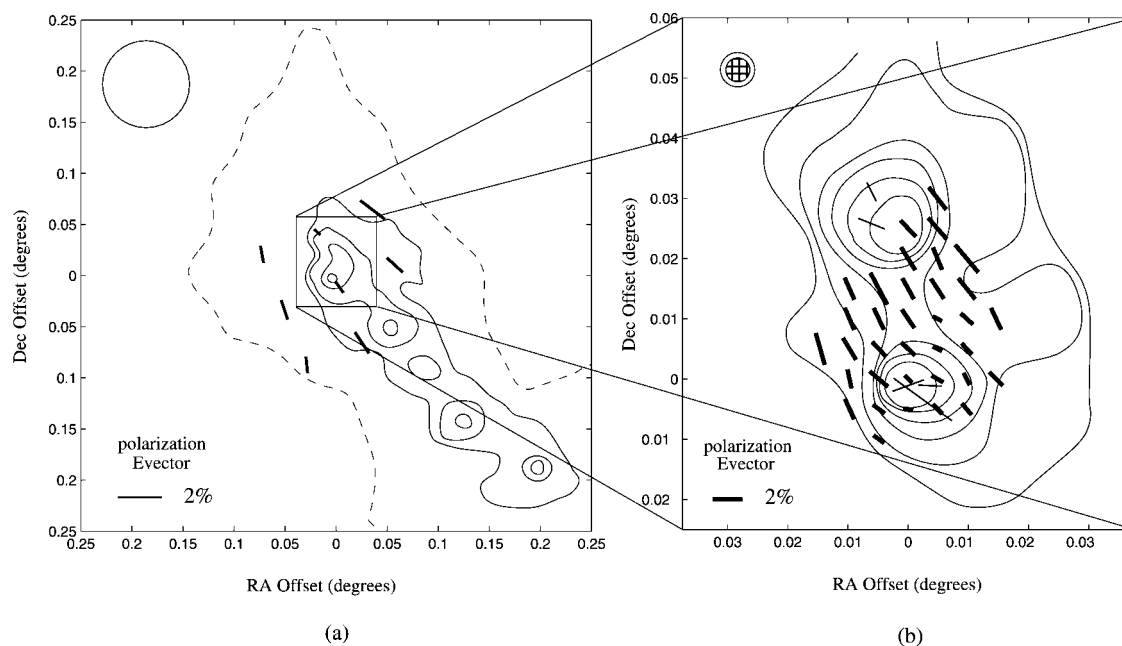
Fig. 4.—Polarimetry of NGC 6334. (*a*) Vectors showing SPARO 450 μm polarization results together with solid contours from the 134 μm intensity map of Loughran et al. (1986). The length of each vector gives the degree of polarization according to the key at lower left, and the direction indicates the measured angle of the *E* vector. SPARO's beam size of approximately 5′ is indicated at upper left. The dashed contour is from a photometric map made with SPARO. (*b*) A view on smaller angular scales (note the lines connecting the two panels). Thin vectors represent JCMT polarimetry (λ = 760 μm; Vallee & Bastien 1999), thick vectors show CSO polarimetry (λ = 350 μm; J. Dotson et al. 2004, in preparation), and contours are from the 400 μm intensity map of Gezari (1982). The intensity map shows two flux peaks, called NGC 6334 I and NGC 6334 I(N). As in (*a*), a scale for the polarization magnitude appears at bottom left, and beam size is indicated at top left for both JCMT polarimetry (grid; 14″) and CSO polarimetry (clear; 20″). The coordinates in each panel give offsets from the peak of NGC 6334 I that is located at 2000 equatorial coordinates ($17^h20^m59^s$, $-35°44'46''$).

nitude of 0.49% and a position angle of 82°. The uncertainty in the SPARO beam size is considered to have negligible effect on the result, because Sgr B2 is strongly peaked. Furthermore, because Sgr B2 is optically thin at λ = 350 μm (Dowell et al. 1998), we estimate that the use of 350 μm data to calibrate our 450 μm observations introduces an error of no more than 0.15%. This upper limit is derived by assuming that the degree of polarization for optically thin emission from dust grains changes no more rapidly than linearly with wavelength (Vaillancourt 2002).

During the SPARO observations of Sgr B2, we took data with the peak of Sgr B2 placed in turn on each of SPARO's 9 pixels. In order to improve the signal-to-noise ratio, these measurements were analyzed as a system of coupled equations linking measured Stokes parameters to instrumental polarizations for all the pixels. A matrix equation was constructed from the system of coupled equations and inverted to isolate the instrumental polarization for each pixel (Chuss 2002).

The second method for deriving the SPARO/Viper instrumental polarization involved observations of the Moon. We assume that it is unpolarized near its center. A similar rastering and matrix inversion procedure was performed for the Moon observations. For a typical pixel, the difference between the

normalized Stokes parameters derived using the two independent calibrators is about 0.2%. The instrumental polarization varied from pixel to pixel, but all pixels have instrumental polarization in the range 0.3%–0.6%.

6. RESULTS FOR NGC 6334

NGC 6334 is a giant molecular cloud with high-mass star formation regions (Cheung et al. 1978; Harvey & Gatley 1982) located 1.7 kpc from the Sun (Neckel 1978). The cloud is elongated parallel to the Galactic plane and has five approximately equally spaced far-infrared sources distributed along its length (see solid contours in Fig. 4*a*). McBreen et al. (1979) labeled these with the roman numerals I–V, where I is northernmost and V southernmost. NGC 6334 I was further resolved into two sources by Gezari (1982), who labeled the northern source I(N), while retaining the I label for the southern source (see contours in Fig. 4*b*).

During 2000 April–July, SPARO obtained polarimetric measurements toward the Galactic center and toward the NGC 6334 I/I(N) complex. We report here on the NGC 6334 observations. The Galactic center observations are discussed by Novak et al. (2003). We also compile other submillimeter polarimetric mea-

surements of NGC 6334 I/I(N) having higher angular resolution but more limited spatial coverage, and we discuss what can be learned by considering these data together with the SPARO data.

6.1. SPARO Observations

SPARO observed NGC 6334 I/I(N) three times during the 2000 austral winter. The total observing time was ~24 hr. These data were combined and corrected for instrumental polarization and for polarization efficiency to produce the final results. We present these polarimetry results in Table 2 and Figure 4a.

Polarized submillimeter radiation from interstellar clouds is usually interpreted as optically thin emission from rotating, elongated, magnetically aligned, cold ($T \sim 30$ K) dust grains. An elongated grain will rotate with its angular momentum vector J parallel to its shortest axis, as this minimizes its energy for a given magnitude of J. The ambient magnetic field provides a natural reference direction for the rotating grain. There are several mechanisms that can align J parallel to the magnetic field direction, including paramagnetic relaxation (Davis & Greenstein 1951) and torques from anisotropic radiation fields (Draine & Weingartner 1997). The emission from the grains is then polarized with the E vector parallel to the long axis of the grain. In this case, the observed direction of polarization will be orthogonal to the projection of the magnetic field onto the plane of the sky. See Lazarian (2000) for a recent review of the theory of grain alignment.

We will at first assume that grains are magnetically aligned with J parallel to the field direction throughout the region we observed. In § 6.3 we discuss alternative interpretations. With the $J \parallel B$ assumption, the SPARO results indicate that the magnetic field in NGC 6334 is generally perpendicular to the elongated ridge of emission (Fig. 4a). This situation is similar to that seen by Dowell et al. (2003) in the high-mass star-forming clouds OMC-1 and DR 21. By carrying out submillimeter polarimetry toward many more such clouds, we can learn whether or not this is a general trend.

6.2. Comparison with CSO/JCMT Observations

Figure 4b shows submillimeter polarimetry of NGC 6334 I/I(N) obtained at $\lambda = 350$ μm using the CSO, and at $\lambda = 760$ μm using the JCMT. A 400 μm intensity map showing the two peaks NGC 6334 I and NGC 6334 I(N) is also shown in this panel. Figure 4b covers only a small sky area located near the center of Figure 4a. Comparing all the polarization data shown in both panels of Figure 4, we see that there is generally good agreement in the direction of all polarization vectors, with a notable exception at the 6334 I flux peak. Here the JCMT result differs from the nearly coincident CSO result by approximately 70°.

It is possible that this discrepancy is caused by differences in the chopper throw (0°.02 for JCMT vs. 0°.10 for CSO data). This is because flux in the reference beams can introduce sys-

TABLE 2
POLARIZATION RESULTS FOR NGC 6334 I

α (hr)	δ (deg)	P (%)	σ_P (%)	ϕ (deg)	σ_ϕ (deg)
17.352	−35.822 ……	0.82	0.40	5.5	14.0
17.348	−35.800 ……	1.24	0.19	33.7	4.4
17.354	−35.768 ……	1.00	0.21	18.3	5.9
17.350	−35.746 ……	0.64	0.10	35.1	4.7
17.345	−35.724 ……	1.06	0.18	47.7	5.0
17.356	−35.714 ……	0.85	0.33	10.2	11.2
17.351	−35.692 ……	0.40	0.13	45.8	9.4
17.347	−35.670 ……	1.51	0.21	52.6	4.1

tematic errors in polarimetry (Schleuning et al. 1997). However, the flux in the vicinity of the NGC 6334 I peak appears very concentrated, so the reference beams may contain relatively little flux. Thus, we will consider other explanations for this discrepancy in polarization angle.

Polarization by absorption has been observed at wavelengths as long as 100 μm in regions having high dust column density (Dowell 1997). Assuming a uniform magnetic field direction, polarization by emission will be perpendicular to polarization by absorption. Because NGC 6334 I has high column density, it seems reasonable to consider whether the near-orthogonality (70° difference) between the CSO and JCMT that results at the peak of NGC 6334 I could be explained by a change in polarization mechanism, between polarization by emission and polarization by absorption.

If the discrepancy is in fact due to this effect, then we have two possibilities: either the 760 μm JCMT result is an effect of absorption and the 350 μm CSO result is from emission, or we have the reverse situation. The first possibility can be ruled out by noting that polarization by absorption is much more efficient at shorter wavelengths (e.g., Dowell 1997). The second possibility can be ruled out by the following argument: the SPARO data extend into the outer regions of the cloud, where 71 μm optical depth measurements of Loughran et al. (1986) indicate low submillimeter optical depth. For example, assuming the grain emissivity law given by Hildebrand (1983), we obtain an optical depth of ~1% at 450 μm. For such low optical depth, polarization by absorption can be ruled out, so the polarization detected by SPARO must be due to the emission mechanism. The CSO polarimetry agrees in direction with the SPARO polarimetry, so it too must be attributed to polarization by emission. We conclude that the 70° discrepancy cannot be explained by a change in polarization mechanism between emission and absorption.

6.3. Discussion

If we assume that the discrepancy in the polarization angles observed toward the peak of NGC 6334 I is not an artifact of differences in chopper throw, then the situation in this cloud is reminiscent of what has been observed in OMC-1. In OMC-1,

which lies at a distance of 500 pc, well-ordered magnetic fields are observed on large angular scales at 100 and 350 μm (Schleuning 1998), but an abrupt, approximately 90° flip in the polarization direction is seen near the flux peak, on angular scales of about 5″ at 1.3 and 3.3 mm (Rao et al. 1998). This is suggestive of a change in mechanism from polarization by emission to polarization by absorption, but polarization by absorption is even less likely at millimeter wavelengths than it is in the submillimeter. Rao et al. consider several possible explanations for the abrupt 90° flip. For example, an anisotropic radiation field can align grains so that their long axes are aligned perpendicular to the photon flux (Harwit 1970). Alternatively, Gold (1952) alignment provides a mechanism to align grains such that they rotate with their long axes parallel to the direction of gas flow. In either of these cases, precession will cause the grains to become aligned either parallel or perpendicular to the magnetic field direction. Thus, a 90° flip could be explained by a change in alignment mechanism.

Invoking one of these two alternate alignment mechanisms for the case of NGC 6334 I might help explain the near-orthogonality of the CSO and JCMT results toward this flux peak. The difference between the CSO and JCMT polarization angles is not quite 90°. However, it is possible that the actual measured difference is a result of neither beam being exactly centered on the region where a putative abrupt 90° change in polarization direction takes place.

Higher angular resolution polarimetry of NGC 6334 I may be able to discriminate among the various possible grain alignment mechanisms. A gradual change in the direction of *P* would suggest that grains are everywhere aligned with *J* parallel to the *B*, with the change in *P* tracing a change in magnetic field morphology. An abrupt 90° flip in direction of *P* could indicate that one of the two alternative alignment mechanisms is operating. In this case, the dust temperature may serve as a discriminant between mechanisms: if the change occurs in a hot region, Gold alignment is more likely. Alignment by photon angular momentum is more likely to be significant in a cold region (Rao et al. 1998).

Based on the highest angular resolution data of NGC 6334 I that is currently available, we tentatively conclude that in fact a gradual change in field direction is being observed. There is some evidence from the CSO data of a slight change in polarization direction near the NGC 6334 I peak, in the sense of agreeing more with the JCMT data. The JCMT data also show evidence of a gradual change, although two of the three data points agree roughly with the polarization direction in the CSO data. Recent submillimeter photometric data suggest that 6334 I has an angular size of 8″–10″ (Sandell 2000). A larger beam size (20″ for CSO vs. 14″ for JCMT) and minor pointing offset (nearest to the peak, CSO points 4″ north of JCMT) may account for the fact that no drastic change in field direction is observed in the CSO data if the changing field direction is contained within the central ~10″ of 6334 I.

In summary, we conclude that in NGC 6334 I, just as in OMC-1, changes in polarization direction occur where massive stars are forming. At present, it is impossible to decide whether this represents a disturbance in the cloud's magnetic field or a change in polarization mechanism, but we have argued that for NGC 6334 I, the former is the more likely possibility.

REFERENCES

Cheung, L., Frogel, J. A., Gezari, D. Y., & Hauser, M. G. 1978, ApJ, 226, L149
Chuss, D. T. 2002, Ph.D. thesis, Northwestern Univ.
Davis, L., & Greenstein, J. L. 1951, ApJ, 114, 206
DeLong, D. E., Smyko, O. G., & Wheatley, J. C. 1971, Rev. Sci. Inst., 42, 147
Dotson, J. L., Novak, G., Renbarger, T., Pernic, D., & Sundwall, J. 1998, Proc. SPIE, 3357, 543
Dowell, C. D. 1997, ApJ, 487, 237
Dowell, C. D., Davidson, J. A., Dotson, J. L., Hildebrand, R. H., Novak, G., Rennick, T. S., Vaillancourt, J. E. 2003, Proc. SPIE, 4843, 250
Dowell, C. D., Hildebrand, R. H., Schleuning, D. A., Vaillancourt, J. E., Dotson, J. L., Novak, G., & Renbarger, T. 1998, ApJ, 504, 588
Draine, B. T., & Weingartner, J. C. 1997, ApJ, 480, 633
Gezari, D. Y. 1982, ApJ, 259, L29
Gold, T. 1952, MNRAS, 112, 215
Gonatas, D. P., Wu, X. D., Novak, G., & Hildebrand, R. H. 1989, Appl. Opt., 28, 1000

Harvey, P. M., & Gatley, I. 1983, ApJ, 269, 613
Harwit, M. 1970, Nature, 226, 61
Hildebrand, R. H. 1983, QJRAS, 24, 267
———. 1985, Opt. Eng., 25, 323
Hildebrand, R. H., Davidson, J. A., Dotson, J. L., Dowell, C. D., Novak, G., & Vaillancourt, J. E. 2000, PASP, 112, 1215
Lane, A. P., 1998, in ASP Conf. Ser. 141, Astrophysics from Antarctica, ed. G. Novak & R. H. Landsberg (San Francisco: ASP), 289
Lazarian, A. 2000, in ASP Conf. Ser. 215, Cosmic Evolution and Galaxy Formation: Structure, Interaction, and Feedback, ed. J. Franco, L. Terlevich, O. López-Cruz, & I. Aretxaga (San Francisco: ASP), 69
Loughran, L., McBreen, B., Fazio, G. G., Rengajaran, T. N., Maxson, C. W., Serio, S., Sciortino, S., & Ray, T. P. 1986, ApJ, 303, 629
Mather, J. C. 1984, Appl. Opt., 21, 1125
McBreen, B., Fazio, G. G., Stier, M., & Wright, E. L. 1979, ApJ, 232, L183
Neckel, T. 1978, A&A, 69, 51

Novak, G., et al. 2003, ApJ, 583, L83
Peterson, J. B., et al. 2000, ApJ, 532, L83
Platt, S. R., Hildebrand, R. H., Pernic, R. J., Davidson, J. A., & Novak, G. 1991, PASP, 103, 1193
Rao, R., Crutcher, R. M., Plambeck, R. L., & Wright, M. C. H. 1998, ApJ, 502, L75
Renbarger, T., Dotson, J. L., & Novak, G. 1998, Appl. Opt., 37, 6643
Ruhl, J. E. 1993, Ph.D. thesis, Princeton Univ.
Ruze, J. 1953, Nuovo Cimento Suppl., 9, 364

Sandell, G. 2000, A & A, 358, 242
Schleuning, D. A. 1998, ApJ, 493, 811
Schleuning, D. A., Dowell, C. D., Hildebrand, R. H., Platt, S. R., & Novak, G. 1997, PASP, 109, 307
Vaillancourt, J. E. 2002, ApJS, 142, 53
Vallee, J. P., & Bastien, P. 1999, ApJ, 526, 819
Ward-Thompson, D., Kirk, J. M., Crutcher, R. M., Greaves, J. S., Holland, W. S., Andre, P. 2000, ApJ, 537, L135
Winston, R. 1970, J. Opt. Soc. Amer., 60, 245